Hindawi
International Journal of Antennas and Propagation
Volume 2023, Article ID 6223384, 14 pages
https://doi.org/10.1155/2023/6223384

Research Article

An Asymmetrical Mixed Higher-Order Discontinuous Galerkin Time Domain Method for Electromagnetic Scattering from the Plasma Sheath around a Hypersonic Vehicle

Jirong Guo and Yiping Han

School of Physics, Xidian University, Xi'an 710071, China

Correspondence should be addressed to Yiping Han; yphan@xidian.edu.cn

Received 15 May 2023; Revised 9 September 2023; Accepted 11 September 2023; Published 26 September 2023

Academic Editor: Paolo Baccarelli

The plasma sheath during reentry of hypersonic vehicle is an unmagnetized and weakly ionized nonuniform plasma flow, which causes radio frequency blackout and strong plasma attenuation of electromagnetic wave. The physical properties of the nonuniform plasma flow were obtained using computational fluid dynamics software with unstructured grids. In this study, a detailed computational model was reconstructed with the high-order Lagrange grids for the nonuniform plasma flow region and the high-order Serendipity grids for the homogeneous medium region. In order to calculate the numerical flux between the two types of grids in the discontinuous Galerkin time domain (DGTD) algorithm, an asymmetric high-order element is constructed as a transition unit. Finally, the simulation results in the plasma sphere show that the above method improves the computational accuracy and decreases calculation. The amplitude and scattering about electromagnetic wave in nonuniform plasma flow are clarified in detail. It is suggested that the presented method could be an effective tool for investigating interaction between electromagnetic waves and plasma flow.

1. Introduction

In recent years, hypersonic weapons near space have played an increasingly important strategic role in warfare. When a hypersonic vehicle reenters the atmosphere, ablative hypersonic viscous flows produces a plasma sheath [1, 2], which is a nonuniform plasma flow composed of free electrons, ions, and neutral particles around hypersonic vehicles [3, 4].

In early research, an approximate method was used to predict the plasma effect, assuming that the plasma flow had a certain electron density distribution. In [5], Rusch simulated the actual plasma sheath profile of the reentry vehicle using a parabolic electron density profile. In [6], a uniform plasma layer was set on the surface of the spherical model to calculate the interaction between the electromagnetic wave and the target. Later, with the development of computer technology, numerical calculation methods such as finite-difference time-domain (FDTD), integral equation method (IEM), and physical optics (PO) were widely used in the study of electromagnetic wave in plasma flow. Basically, the simulations of interactions between the plasma and electromagnetic wave are performed by using the particle-in-cell method, which is based on the finite difference time domain (FDTD) method [7, 8] or the FDTD method combined with the effective permittivity model.

In [9], the physical optics method was used to calculate the scattering characteristics of the electromagnetic wave in inhomogeneous plasma sheath from the S-band to the Ku-band frequencies. In [10], a well-conditioned internally combined volume surface integral equation (ICVSIE) for analyzing electromagnetic scattering from perfect electrically conducting (PEC) surfaces coated with negative permittivity plasmas is presented to be applied in various canonical scatterers and a plasma-engulfed reentry vehicle. Scarabosio et al. employ the Eikonal approximation in the large inhomogeneous plasma region [11] and compute radiation and scattering via the equivalence theorem, and the results show

that significant radio link path losses can be associated with plasma spatial variations (gradients) and collisional losses. In [12], the Drude mode is proven to be adopted to characterize collisional plasma. In the calculation with FDTD, radar cross section (RCS) of nonuniform plasma spheres and conductor spheres coated by the plasma layer are calculated. A piecewise linear JE recursive convolution finite-difference time-domain (PLJERC-FDTD) was used to study the scattering characteristics of electromagnetic waves in time-varying and inhomogeneous plasma sheath [13]. In [14], the high-order FDTD method was used to simulate the RCS (radar cross section) from the plasma flow in a shock tube. To increase the computational efficiency, Chen and Wang et al. used the hybrid-implicit-explicit (HIE)-FDTD method [15, 16] to simulate the gyrotropic plasma in open regions [17]. Chen and Wang proposed to apply the weakly conditionally stable (WCS)-FDTD method [18] to simulate the plasma frequency selective surface [19]. Numerical experiments showed that both the HIE-FDTD and WCS-FDTD methods can enhance significantly the computational efficiency of plasma simulations. However, because of the used Yee cell, the FDTD methods suffer from serious accuracy deterioration when they come to irregular objects.

In [20], electromagnetic wave behavior in plasma with the combined CFD and FD2TD method was investigated. The distribution of charged particles around the ESA ARD and the complicated behavior of electromagnetic waves, with attenuation and reflection, are clarified in detail.

For DGTD analysis, elements in tetrahedral form can be better fit to irregular objects [21, 22]. In [23], DGTD is used to solve electromagnetic scattering from hypersonic aircraft with plasma sheath; however, the flight status and the specific parameters of the plasma sheath were not given in the paper. In [24], an exponential-based DGTD method for the 3-D modeling of hypersonic vehicles with surrounded by a uniform plasma layer is presented, and this method enables the usage of larger time steps compared with the explicit time marching scheme. In the above-mentioned DGTD methods, tetrahedral elements are used in the computational domain, which is inefficient when calculating complex geometric objects. More recently, the DGTD with hexahedron have attracted extensive attention for modeling with complex geometrical features [25]. In [26], DGTD with the high-order basis function is proposed to solve electromagnetic scattering from hypersonic aircraft with plasma sheath in which dielectric parameter changes with frequency, respectively. A hybrid mesh DGTD algorithm based on virtual elements for tetrahedra and hexahedra is proposed to improve the computational efficiency [27]. But tetrahedra and hexahedra are applied in different subdomains, respectively.

In this study, the Lagrange high-order element is used to read more plasma parameters in the plasma flow region, the efficient Serendicity high-order element is used in the uniform medium area, and the asymmetric high-order elements are constructed as the transition units between two types of elements to calculate the numerical flux. The high-order points of the Serendicity high-order element close to the shape of aircraft can be mapped to aircraft surface by isoparametric element. This article is organized as follows. In Section 2, time-domain Maxwell's equations in the Drude dispersive medium are presented. Section 3 describes the physical and numerical models of asymmetric mixed higher-order mesh. As far as the authors' knowledge, this is the first time that an asymmetric mixed higher-order mesh DGTD method is developed for the numerical simulation of nonuniform plasma flow target. Finally, numerical experiments of scattering problems are presented in Section 4, and the accuracy of the proposed method is verified through comparison with the results of Mie theory. It was confirmed that plasma flow under different flight altitudes has different effects on electromagnetic scattering.

2. Iterative Equation of DGTD

We recall the propagation of an electromagnetic wave in the dispersive medium. We can use the dielectric coefficient to express the characteristics of the nonmagnetized medium. The dielectric coefficient related to frequency can be given by

$$\varepsilon(\omega) = \varepsilon_0\left[\varepsilon_r'(\omega) - j\varepsilon_r''(\omega)\right] = \varepsilon_0\left[\varepsilon_\infty + \chi(\omega)\right], \tag{1}$$

where ε_∞ is the relative dielectric constant at infinity frequency, ε_0 is the dielectric coefficient in vacuum, and χ_ω is the polarizability function.

2.1. Drude Dispersive Medium. The nonuniform plasma flow of hypersonic vehicles is usually treated as cold plasma, which is expressed by the Drude dispersive medium. The thermochemical nonequilibrium model is used in computational fluid dynamics (CFD) to simulate the nonuniform plasma flow. The concentration of electrons, density of neutral particles, and temperature in the nonuniform plasma flow are important parameters for calculating the dielectric coefficient. In the Drude dispersive medium [28], χ_ω is given by

$$\chi(\omega) = -\frac{\omega_p^2}{\omega\left(\omega - j\upsilon_c\right)}, \tag{2}$$

where ω_p is the plasma collision frequency and ν_c is the plasma frequency which are given by

$$\omega_p = \sqrt{\frac{n_e e^2}{m_e \varepsilon_0}}, \qquad \upsilon_c = n_s \sigma_{\text{es}} \sqrt{\frac{8\kappa T_\nu}{\pi m_e}}, \tag{3}$$

where m_e is the electron mass, n_e is the number density of electrons, n_s is the number density of species s, e is the magnitude of the electronic charge equal to 4.80298×10^{-10}esu, and k is Boltzmann's constant. The effective electron-neutral energy exchange cross section is defined by a curve fit of the form.

$$\sigma_{\text{es}} = \tilde{a}_s + \tilde{b}_s T_e + \tilde{c}_s T_e^2. \tag{4}$$

The constants for equation (4) are presented in Table 1.

2.2. Formulation in Computational Domain. The Maxwell equations are

$$\begin{aligned} \nabla \times E &= -\frac{\partial B}{\partial t} - \sigma_m H, \\ \nabla \times H &= \frac{\partial D}{\partial t} + \sigma E, \\ B &= \mu H, \\ D(\omega) &= \varepsilon(\omega) E(\omega). \end{aligned} \tag{5}$$

Substituting equation (1) into equation (5), we obtain

$$\begin{aligned} \nabla \times H &= \varepsilon_0 \varepsilon_\infty \frac{\partial E}{\partial t} + \varepsilon_0 \chi(\omega) \frac{\partial E}{\partial t} + \sigma E \\ &= \varepsilon_0 \varepsilon_\infty \frac{\partial E}{\partial \mathrm{t}} + J_P(\omega) + \sigma E. \end{aligned} \tag{6}$$

Space Ω is divided into nonoverlapping and continuous subregions. Each subregion is a separate hexahedral element, and its weight function (also called basis function) is ϕ_i (i is the serial number of the unit). The weighted integral of equation (6) in each element is taken and set equal to zero, such that

$$\begin{aligned} \int_{V_i} \left[\frac{\partial}{\partial t} \mu H + \sigma_m H + \nabla \times E \right] \cdot \phi_{\mathrm{i}} \mathrm{dv} = 0, \\ \int_{V_i} \left[\frac{\partial}{\partial t} \varepsilon \varepsilon_\infty E + J_P(\omega) + \sigma E - \nabla \times H \right] \cdot \phi_{\mathrm{i}} \mathrm{dv} = 0, \end{aligned} \tag{7}$$

Table 1: Constants for curve fits of electron-neutral energy exchange cross section σ_{es}.

s	$\widetilde{a}_s$	$\widetilde{b}_s$	$\widetilde{c}_s$
N	$5E-20$	0	0
O	$1.2E-20$	$1.7E-24$	
N_2	$7.5E-20$	$5.5E-24$	$-2E-29$
O_2	$2E-20$	$6E-24$	$-1E-28$
NO	$1E-19$	0	0

where ϕ_i is the weight function. The numerical fluxes are defined at the boundary between two elements as

$$\begin{aligned} n^i \times E^{i^*} &= n^i \times E^i + \kappa_e^i \left[n^m \times \left(E^{i+} - E^i \right) + M_S \right] \\ &\quad + \nu_h^i \left[n^i \times \left(n^i \times \left(H^{i+} - H^i \right) - J_S \right) \right], \\ n^i \times H^{i^*} &= n^i \times H^i + \kappa_h^i \left[n^m \times \left(H^{i+} - E^i \right) - J_S \right] \\ &\quad - \nu_e^i \left[n^i \times \left(n^i \times \left(E^{i+} - E^i \right) + M_S \right) \right], \end{aligned} \tag{8}$$

where $\widehat{n}$ is the unit outward normal vector in each surface of the element, $\mathbf{E}^*$ and $\mathbf{H}^*$ are the numerical fluxes, $\mathbf{E}^+$ and $\mathbf{H}^+$ are in the fields of the adjacent element, and $\mathbf{E}$ and $\mathbf{H}$ are in the fields of the element. κ_e, κ_h, υ_e, and υ_h are presented in Table 2.

$$\begin{aligned} \int_{V_i} (\nabla \times E) \cdot \phi_i \mathrm{dv} &= \int_{V_i} (\nabla \times E) \cdot \phi_i \mathrm{dv} + \oint_{\partial V_i} \kappa_e^i \left[n^m \times \left(E^{i+} - E^i \right) + M_S \right] \mathrm{ds} \\ &\quad + \oint_{\partial V_i} \nu_h^i \left[n^i \times \left(n^i \times \left(H^{i+} - H^i \right) - J_S \right) \right] \mathrm{ds}, \\ \int_{V_i} (\nabla \times H) \cdot \phi_i \mathrm{dv} &= \int_{V_i} (\nabla \times \phi_i) \cdot H \mathrm{dv} - \oint_{\partial V_i} \kappa_h^i \left[n^m \times \left(H^{i+} - E^i \right) - J_S \right] \mathrm{ds} \\ &\quad + \oint_{\partial V_i} \nu_e^i \left[n^i \times \left(n^i \times \left(E^{i+} - E^i \right) + M_S \right) \right] \mathrm{ds}. \end{aligned} \tag{9}$$

Substituting (9) into (7), we obtain

Table 2: Numerical flux coefficient.

Numerical flux	κ_e	κ_h	υ_e	υ_h
Centered flux	1/2	1/2	0	0
Upwind flux	$Y^+/Y + Y^+$	$Z^+/Z + Z^+$	$1/Y + Y^+$	$1/Z + Z^+$

$$\begin{aligned}
&\int_{V_i} \mu \frac{\partial H}{\partial t} \cdot \phi_i \mathrm{d}v + \int_{V_i} \sigma_m H \cdot \phi_i \mathrm{d}v + \int_{V_i} (\nabla \times E) \cdot \phi_i \mathrm{d}v \\
&+ \oint_{\partial V_i} \kappa_e^i \left[n^m \times \left(E^{i+} - E^i \right) + M_S \right] \cdot \phi_i \mathrm{d}s \\
&+ \oint_{\partial V_i} \nu_h^i \left[n^i \times \left(n^i \times \left(H^{i+} - H^i \right) - J_S \right) \right] \cdot \phi_i \mathrm{d}s = 0, \\
&\int_{V_i} \varepsilon \varepsilon_\infty \frac{\partial E}{\partial t} \cdot \phi_i \mathrm{d}v + \int_{V_i} J_P(\omega) \cdot \phi_i \mathrm{d}v \\
&+ \int_{V_i} \sigma E \cdot \phi_i \mathrm{d}v - \int_{V_i} (\nabla \times H) \cdot \phi_i \mathrm{d}v \\
&- \oint_{\partial V_i} \kappa_h^i \left[n^m \times \left(H^{i+} - E^i \right) - J_S \right] \cdot \phi_i \mathrm{d}s \\
&+ \oint_{\partial V_i} \nu_e^i \left[n^i \times \left(n^i \times \left(E^{i+} - E^i \right) + M_S \right) \right] \cdot \phi_i \mathrm{d}s = 0.
\end{aligned} \tag{10}$$

3. Asymmetrically Mixed Higher-Order Mesh

The aircraft is a RAM-CII aircraft scaling model in this paper. The nonuniform flow is simulated by FASTRAN whose numerical algorithm is the finite volume method based on density [29].

In Figure 1, the plasma flow forms a viscous boundary layer on the aircraft surface when flight altitude is 55 km and velocity altitude is 20 Mach, and the plasma parameters have a large gradient. The maximum value of plasma frequency ω_p appears in the area of the blunt cone head (with an order of magnitude of $2\pi \times 10^{11}$rad/s), and the closer to the blunt cone head, the greater the value of plasma frequency ω_p (as shown in Figure 1(a). The plasma frequency in the other regions decreased approximately one order of magnitude, about $2\pi \times 10^{10}$rad/s. The maximum value of the collision frequency of υ_c appears in the area of the blunt cone head, with an order of magnitude of $2\pi \times 10^{10}$rad/s (as shown in Figure 1(b)). The collision frequency υ_c in the other regions decreased approximately one order of magnitude around $2\pi \times 10^{10}$rad/s.

A detailed computational model was reconstructed with mixed high-order hexahedral grids for the DGTD code. In order to read more parameters of the nonuniform plasma flow, the electromagnetic model is divided by mixed high-order hexahedral grids.

A hexahedral element constructs the basis function through isoparametric elements [30, 31]. The nodes of the actual mesh and isoparametric cell are in one-to-one correspondence, as shown in Figure 2. Construct three isoparametric unctions (as shown in Figures 2(a)–2(c)) for three actual unctions (as shown in Figures 2(d)–2(f)) defined over the square $\{(\xi, \eta, \zeta) \mid -1 < \xi, \eta, \zeta < 1\}$.

The isoparametric element is the standard element in $\xi\eta\zeta$ coordinates. If there are n basis functions, they can be given by

$$\begin{aligned}
&N_i\left(\xi_j, \eta_j, \zeta_j\right) = \begin{cases} 1, & i = j, \\ 0, & i \neq j, \end{cases} \\
&\sum_{i=1}^{m} N_i(\xi, \eta, \zeta) = 1.
\end{aligned} \tag{11}$$

The basis function ϕ_i satisfies the abovementioned conditions, and the mapping formula from local coordinates to actual coordinates is as follows:

$$\begin{aligned}
x &= \sum_{i=1}^{n} x_i \phi_i\left(\xi_j, \eta_j, \zeta_j\right), \\
y &= \sum_{i=1}^{n} y_i \phi_i\left(\xi_j, \eta_j, \zeta_j\right).
\end{aligned} \tag{12}$$

The isoparametric element can be mapped to element with arbitrary shape using the abovementioned formula. In the higher-order element, the right-angle edge of the standard element can be mapped to the parabolic boundary of the actual element.

In Figure 3, the 27 nodes high-order Lagrange element is used in the nonuniform plasma flow, which can read more plasma parameters by using more internal nodes. The efficient 20 nodes Serendipity element is used in the homogeneous medium region, which has no internal nodes, thus ensuring the accuracy of calculation and reducing the amount of computation. In order to calculate the numerical flux between the two types of elements in the DGTD algorithm, an asymmetric high-order element is constructed as a transition unit.

3.1. NonUniform Plasma Flow Region Mesh. Lagrange high-order element is used in the nonuniform plasma flow region. It is assumed that the isoparametric element is divided into $r + 1$ groups, $p + 1$ groups, and $t + 1$ groups of nodes in the x, y, and z directions, respectively, and the nodes are located at the intersection lines of the element. Node i is located in groups m, n, and k in the x, y, and z directions, respectively. Its interpolation functions are

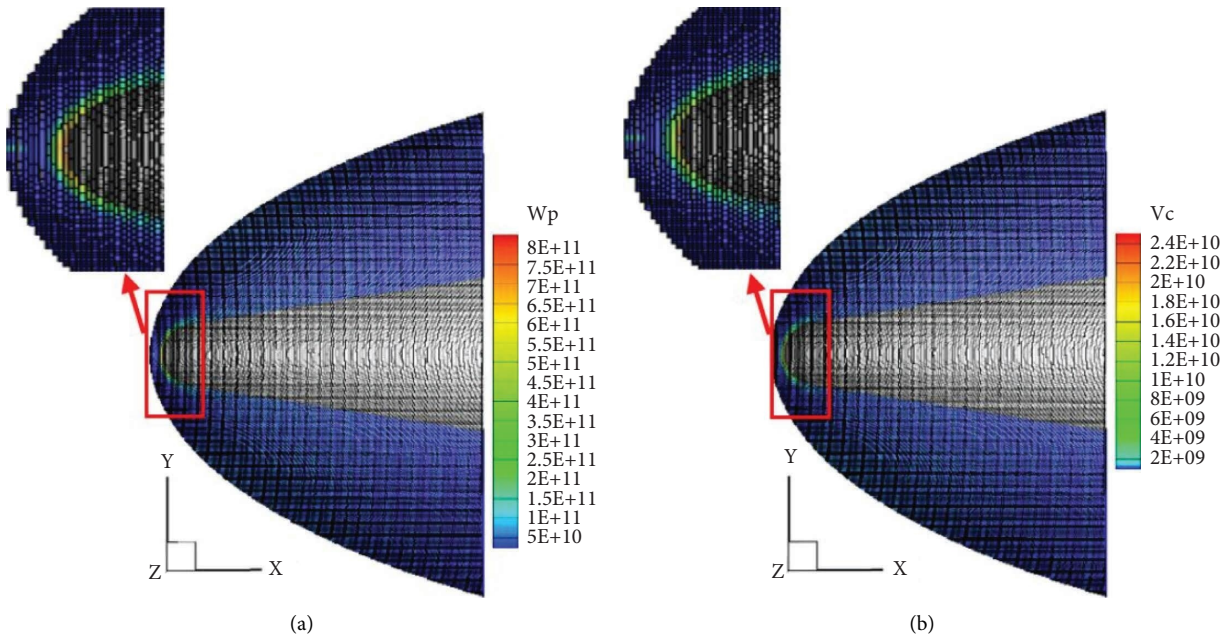

FIGURE 1: The distribution of plasma collision frequency and plasma frequency in the plasma flow field at the flight altitude of 55 km and the flight speed of 20 ma.

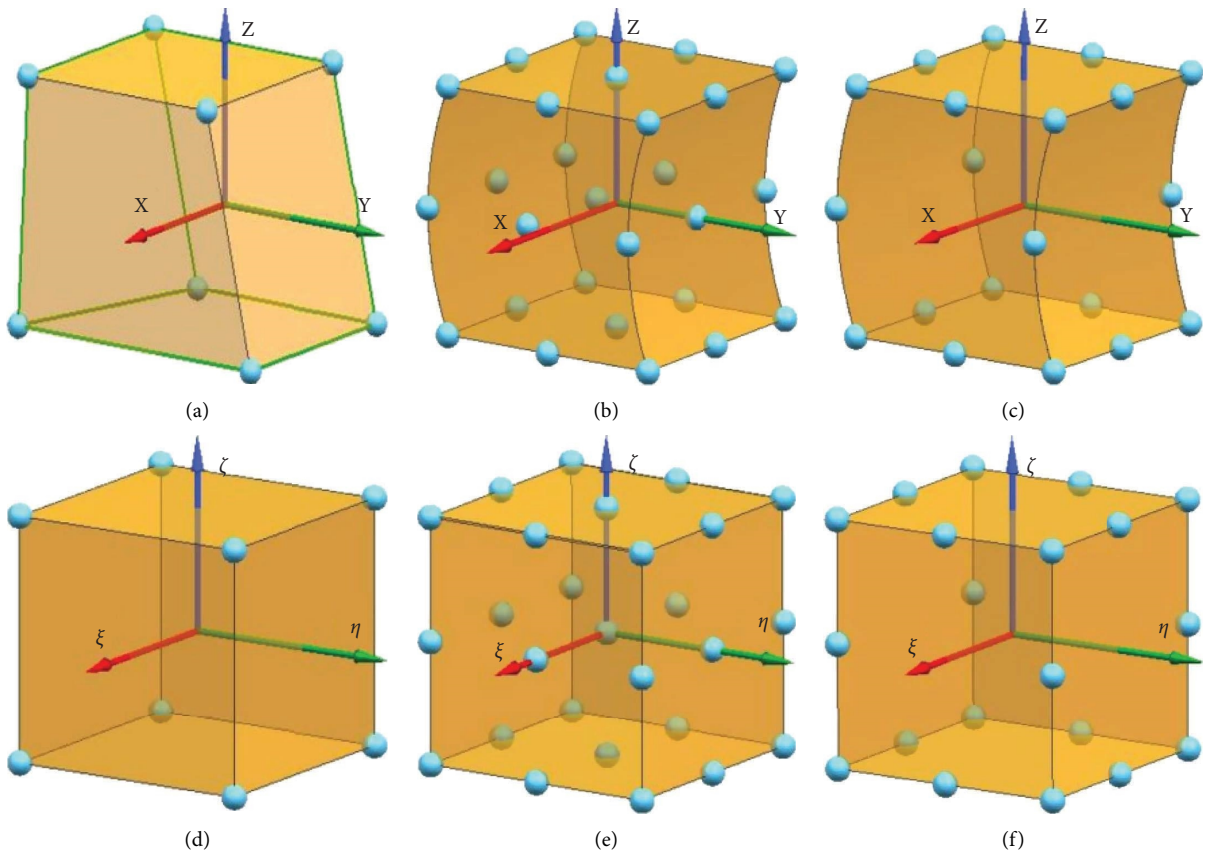

FIGURE 2: The hexahedral elements: (a) arbitrary 8 nodes hexahedron; (b) 27 nodes lagrange high-order element\%; (c) 20 nodes serendipity high-order element; (d) 8 nodes isoparametric element; (e) 27 nodes isoparametric element; (f) 20 nodes isoparametric element.

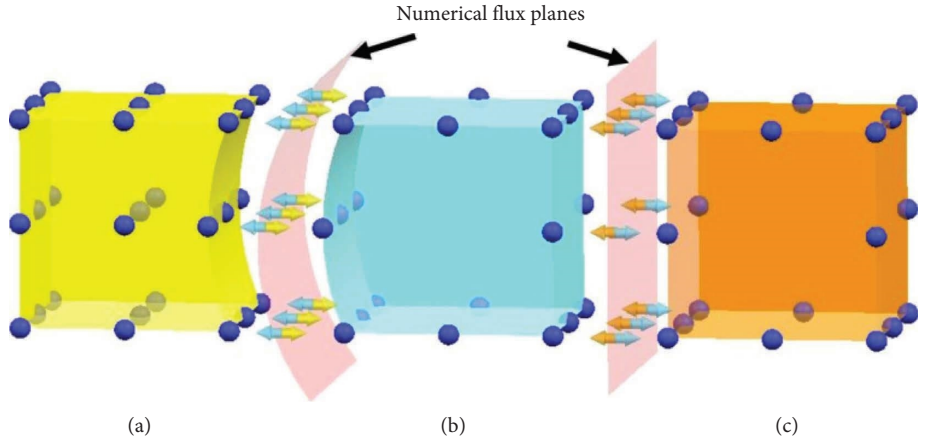

Figure 3: A transition unit between two types of elements (a) 27 nodes Lagrange element, (b) the asymmetric high-order element, and (c) 20 nodes serendipity element.

$$
\begin{aligned}
l_m^r(\xi) &= \frac{(\xi-\xi_1)(\xi-\xi_2)\cdots(\xi-\xi_{m-1})(\xi-\xi_{m+1})\cdots(\xi-\xi_r)}{(\xi_m-\xi_1)(\xi_m-\xi_2)\cdots(\xi_m-\xi_{m-1})(\xi_m-\xi_{m+1})\cdots(\xi_m-\xi_r)},\\
l_n^p(\eta) &= \frac{(\eta-\eta_1)(\eta-\eta_2)\cdots(\eta-\eta_{n-1})(\eta-\eta_{n+1})\cdots(\eta-\eta_p)}{(\eta_n-\eta_1)(\eta_n-\eta_2)\cdots(\eta_n-\eta_{n-1})(\eta_n-\eta_{n+1})\cdots(\eta_n-\eta_p)},\\
l_k^t(\zeta) &= \frac{(\zeta-\zeta_1)(\zeta-\zeta_2)\cdots(\zeta-\zeta_{k-1})(\zeta-\zeta_{k+1})\cdots(\zeta-\zeta_t)}{(\zeta_k-\zeta_1)(\zeta_k-\zeta_2)\cdots(\zeta_k-\zeta_{k-1})(\zeta_k-\zeta_{k+1})\cdots(\zeta_k-\zeta_t)}.
\end{aligned}
\tag{13}
$$

The basis function N_i of node i can be obtained by multiplying the Lagrange polynomials in the above:

$$
N_i = l_m^r(\xi)\cdot l_n^p(\eta)\cdot l_k^t(\zeta). \tag{14}
$$

Grid-generation software usually provides only the first order nodes of an element. In order to effectively fit the higher order element nodes near the boundary of the plasma flow to the contour of the plasma flow, we set more surface points of the plasma flow region as mapping points of the higher-order element by constructing a cylindrical coordinate system.

$$
\begin{cases}
r = \sqrt{x^2+y^2},\\
\theta = \arctan\dfrac{x}{y},\\
Z = z.
\end{cases}
\tag{15}
$$

Firstly, the surface mesh of the flow region is further subdivided separately. The further subdivided mesh is denser than the working mesh as shown in Figure 4(b).

Then, the cylindrical coordinate system $r\theta Z$ in Figure 4 is established in the further mesh. The actual coordinate points and the higher-order grid nodes close to the flow field have the same values on the Z and θ axes (as shown in Figure 5). The transformation relationship between the cylindrical coordinate system and the rectangular coordinate system is as follows:

Finally, a suitable cylindrical surface point is found according to the value of Z axis and θ axis corresponding to the higher-order node.

3.2. Uniform Medium Region Mesh. The uniform medium region is divided by the Serendipity high-order element. The Serendipity higher-order element is shown in Figure 3(c), whose basis functions are

$$
\begin{aligned}
N_i &= \frac{1}{8}(1+\xi_i\xi)(1+\eta_i\eta)(1+\zeta_i\zeta)(\xi_i\xi+\eta_i\eta+\zeta_i\zeta-2) \quad (\xi_i\neq 0,\eta_i\neq 0,\zeta_i\neq 0),\\
N_i &= \frac{1}{4}(1-\xi^2)(1+\eta_i\eta)(1+\zeta_i\zeta) \quad (\xi_i=0,\eta_i=\pm 1,\zeta_i=\pm 1),\\
N_i &= \frac{1}{4}(1-\eta^2)(1+\xi_i\xi)(1+\zeta_i\zeta) \quad (\eta_i=0,\xi_i=\pm 1,\zeta_i=\pm 1),\\
N_i &= \frac{1}{4}(1-\zeta^2)(1+\eta_i\eta)(1+\xi_i\xi) \quad (\zeta_i=0,\eta_i=\pm 1,\xi_i=\pm 1).
\end{aligned}
\tag{16}
$$

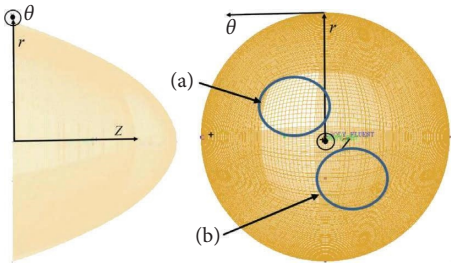

Figure 4: Cylindrical coordinate system (a) working element (b) further element.

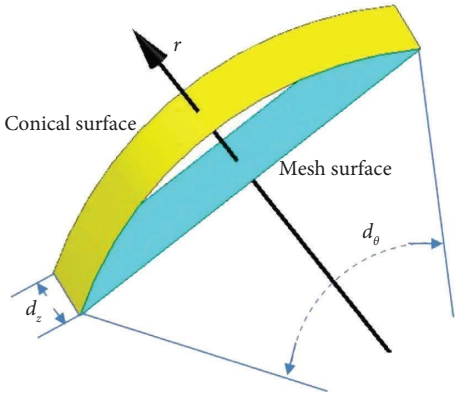

Figure 5: A point of the element map to cylindrical coordinate.

3.3. Transition Unit (Asymmetric High Order Element). The Lagrange high-order element with 27 nodes and the Serendipity high-order element with 20 nodes are used in this paper. There are 9 nodes at each face of the Lagrange high-order element and 8 nodes at each face of the Serendipity high-order element. An asymmetric high-order element with 21 nodes is constructed as a transition element (as shown in Figure 6).

To determine the arbitrary basis function N_i as follows, we divide n planes that do not pass through node i but pass through all other nodes of the element.

$$N_i(\xi,\eta,\zeta) = \frac{\prod_{k=1}^{n} F_k(\xi,\eta,\zeta)}{\prod_{k=1}^{n} F_k(\xi_i,\eta_i,\zeta_i)} \quad F_k = 0\,, \quad k = 1\cdots n. \tag{17}$$

Next, the basis function of the asymmetric higher-order element is constructed. First, high-order node 21 $(\xi = 0, \eta = 0, \zeta = 1)$ is constructed on the basis of 20 nodes Serendipity high-order element. N_{21} is given by

$$N_{21} = \frac{1}{2}\left(1-\xi^2\right)\left(1-\eta^2\right)(1-\zeta). \tag{18}$$

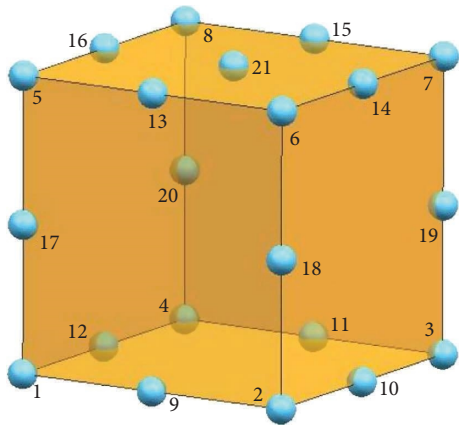

Figure 6: Transition element.

Firstly, we assume that the basic functions of a 20-nodes Serendipity higher-order grid are $N_1' \sim N_{20}'$. Substitute $N_1' \sim N_{20}'$ and N_{21} into the displacement function [32]:

$$u(x,y,z) = N_1'u_1 + N_2'u_2 + \cdots N_{20}'u_{20} + N_{21}'u_{21}. \tag{19}$$

Substitute $\xi = 0, \eta = 0, \zeta = 1$ into equation (19)

$$u(x,y,z)|_{\xi=0,\eta=0,\zeta=1} = \frac{1}{2}u_{13} + \frac{1}{2}u_{14} + \frac{1}{2}u_{15} + \frac{1}{2}u_{16} - \frac{1}{4}u_5 - \frac{1}{4}u_6 - \frac{1}{4}u_7 - \frac{1}{4}u_8 + u_{21}. \tag{20}$$

Then, we can get u'_{21} as

$$u'_{21} = u_{21} - \left(\frac{1}{2}u_{13} + \frac{1}{2}u_{14} + \frac{1}{2}u_{15} + \frac{1}{2}u_{16} - \frac{1}{4}u_5 - \frac{1}{4}u_6 - \frac{1}{4}u_7 - \frac{1}{4}u_8 + u_{21}\right). \tag{21}$$

Finally, substitute u'_{21} instead of u_{21} into the displacement function:

$$\begin{aligned} u(x,y) = {} & N'_1 + N'_2 \cdots \\ & + \left(N'_5 + \frac{1}{4}N_{21}\right)u_5 + \left(N'_6 + \frac{1}{4}N_{21}\right)u_6 \cdots \\ & + \left(N'_7 + \frac{1}{4}N_{21}\right)u_7 + \left(N'_8 + \frac{1}{4}N_{21}\right)u_8 \cdots \\ & + \left(N'_{13} - \frac{1}{2}N_{21}\right)u_{13} + \left(N'_{14} - \frac{1}{2}N_{21}\right)u_{14} \cdots \\ & + \left(N'_{15} - \frac{1}{2}N_{21}\right)u_{15} + \left(N'_{16} - \frac{1}{2}N_{21}\right)u_{16} \cdots \\ & + N'_{20}u_{20} + N_{21}u_{21}, \end{aligned}$$

$$N_i = \begin{cases} N'_i & \begin{pmatrix} i = 1,2,3,4,9,10,11,12, \\ 17,18,19,20,21 \end{pmatrix}, \\ N'_i + \frac{1}{4}N_{21}, & (i = 5,6,7,8), \\ N'_i - \frac{1}{2}N_{21}, & (i = 13,14,15,16). \end{cases} \tag{22}$$

All basis functions can be deduced in terms of the abovementioned way.

4. Examples

In the following, two numerical experiments are used to verify the effectiveness of the asymmetrically mixed high-order mesh DGTD method, and the influence of nonuniform plasma flow on electromagnetic scattering is discussed.

4.1. RCS of a Plasma Sphere. We calculate the monostatic radar cross section (RCS) of a plasma ball ($\omega_p = 2\pi \times 28.7 \times 10^9$rad/s, $v_c = 2.0 \times 10^{10}$Hz, $r = 3.75$ mm). In the case of mixed higher order element, the plasma sphere mesh is mapped to 27 nodes second-order Lagrange element, and the other mesh is mapped to 20 nodes second-order Serendipity element, an asymmetric high order element with 21 nodes is constructed as a transition unit between two types of elements.

As shown in Figure 7, a very good agreement is achieved among the results obtained using the mixed higher-order element method, second-order Lagrange element method, and the Mie theory. Compared with DGTD with the first order element, this method has less RCS error, especially when the frequency is 76.2 GHz, 93.5 GHz (as shown in Table 3).

4.2. RCS of Inhomogeneous Plasma Flow around Blunt Cone. In this example, monostatic and bistatic radar cross section (RCS) of the blunted cone surrounded by nonuniform plasma flow is illuminated. We consider a Gaussian pulse incidents from the front of the blunted cone ($\theta = 90, \phi = 0$). The blunted cone has a blunted nose of radius 0.01 m, a conical cross section with half-angle of 9°, and a whole length 0.1 m.

As shown in Figure 8, the 3D geometric model is divided by the hexahedral grids consists of 1067631 hexahedrons. Table 4 shows the memory required and calculation times of 27 nodes Lagrange mesh and mix-order mesh with 8 parallel threads algorithm. The results demonstrate that mix-order mesh is more efficient, with the required memory being reduced by 26.85%. To truncate the open boundary of the simulation, the uniaxial perfectly matched layer (UPML) with a thickness of 0.0032 m is placed at least 0.006 m away from the plasma sheath.

In Figure 9, the influence of flight altitude and Mach number on the backward RCS of blunt cones at altitudes of 50 and 55 km and speeds of 20 Mach are analyzed. When the frequency is below 1.8 GHz, the plasma flow enhances the

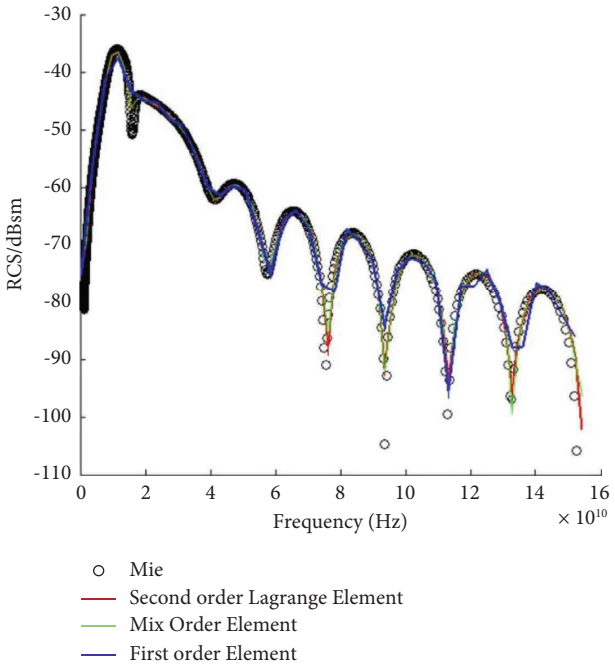

Figure 7: Backward scattering of the plasma sphere.

Table 3: RCS error of mix order element and first order element.

	76.2 GHz	93.5 GHz[a]
Mix order element	1.53dBsm	0.08dBsm
First order element	12.81dBsm	10.17dBsm

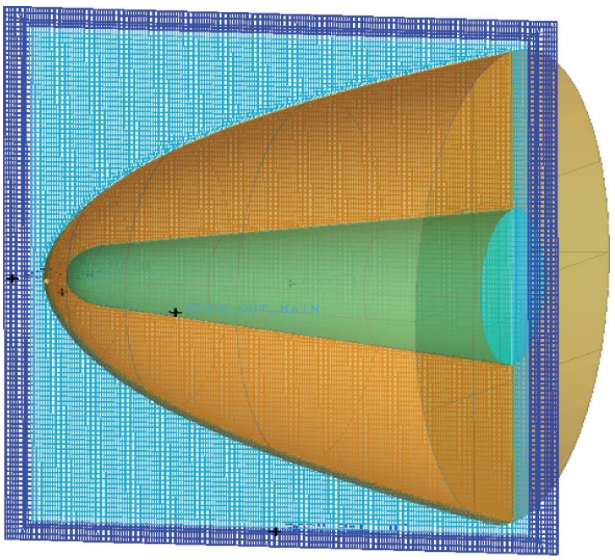

Figure 8: Computational model.

Table 4: Parameter records for both meshes.

	Memory (GB)	Calculation time (h)[a]
27 nodes lagrange mesh	68.25	17.8
Mix-order mesh	49.92	18.1

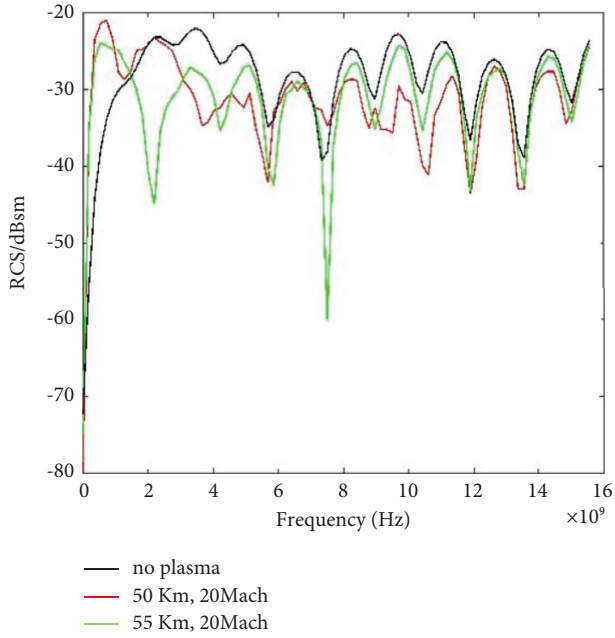

Figure 9: RCS of the plasma sphere.

backward RCS of the blunt cone greatly. When the collision frequency is greater than the incident wave frequency, reducing the incident wave frequency will increase reflection [33]. When the frequency is 1.8 GHz~13 GHz, the plasma flow will reduce the backward RCS of blunt cone. When the frequency is above 13 GHz, the backward RCS of blunt cone with plasma is consistent with that without plasma, indicating that the plasma flow has little influence on the electromagnetic scattering of the reentry target in the high frequency band.

Aiming at abovementioned characteristics, we discuss the bistatic RCS and the electric field amplitude of the nonuniform flow field target, which is at the altitude of 55 km and the velocity of 20 Mach with three frequency bands of 1.0 GHz, 4.0 GHz, and 15.0 GHz.

The amplitude at 1.0 GHz without and with the plasma flow of XOZ section is given in Figures 10(a) and 10(b). When the frequency is 1.0 GHz, the incident wave cannot penetrate the plasma flow near the nose as show in the partial enlarged view. In the plasma layer near the nose, the blue shadow in Figure 10(b) increases compared to Figure 10(a). Therefore, the backward and lateral RCS of the blunt cone with plasma flow, particularly in 50 km 20 Mach condition, are greater than that of the blunt cone without plasma flow in Figure 10(c). The interaction between the plasma flow and the incident wave is more obvious, as the altitude decreases.

When the frequency of the incident wave increases to 4.0 GHz, the lateral RCS of the blunt cone with plasma flow are smaller than that of the blunt cone without plasma flow, particularly in 50 km 20 Mach condition, the backward RCS is the reverse of the lateral RCS (as shown Figure 11(c)). Compared with Figure 11(a), the effect of plasma flow on incident waves is relatively strong in Figure 11(b).

When the frequency of the incident wave is 15.0 GHz, the incident wave can penetrate the plasma flow. The influence of plasma flow on amplitude decreases in Figure 12(b). The RCS of the blunt cone with plasma flow is close to that without plasma flow, particularly in 55 km 20 Mach condition (as shown in Figure 12(c)).

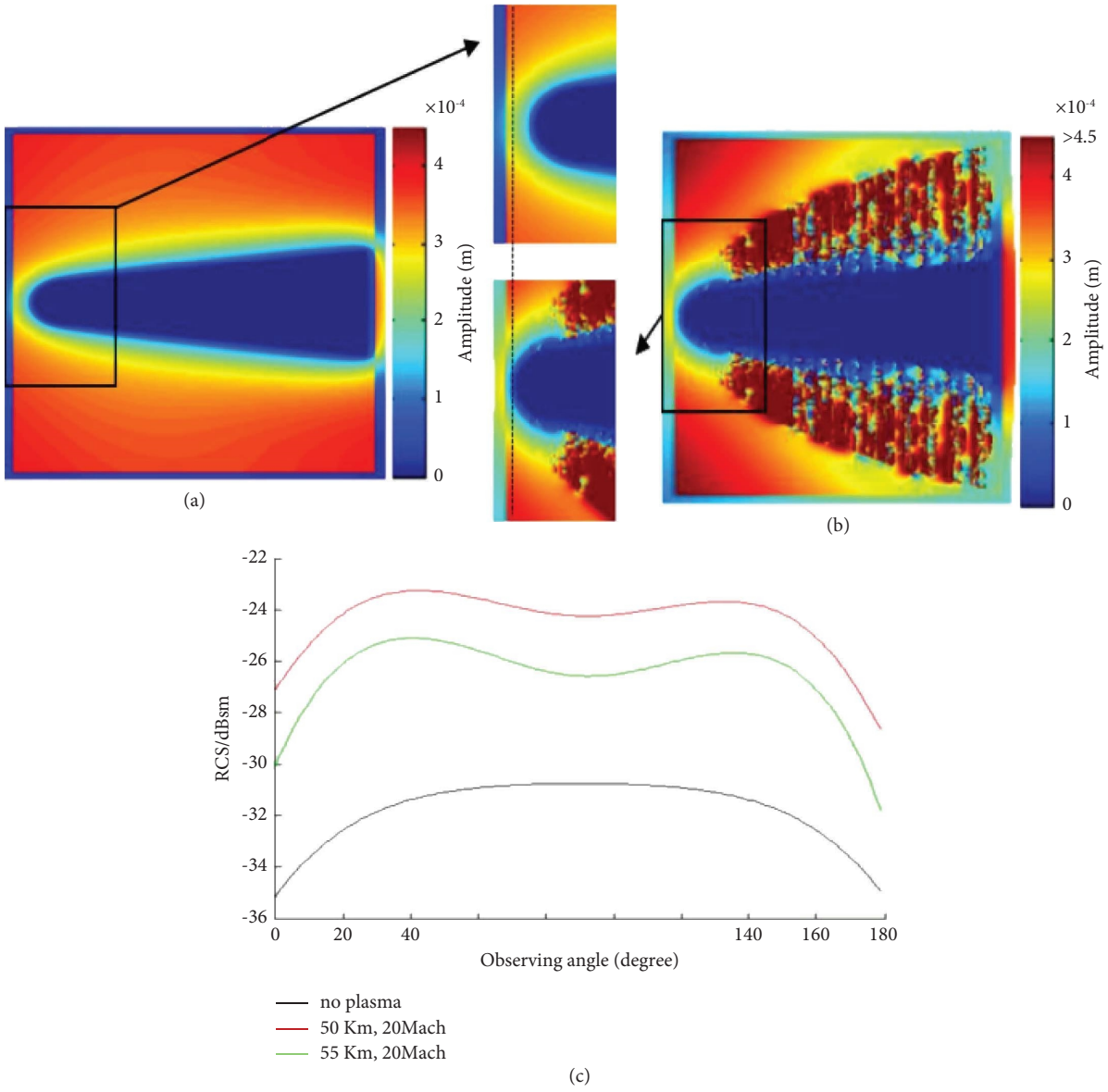

Figure 10: The amplitude and bistatic RCS at 1.0 GHz.

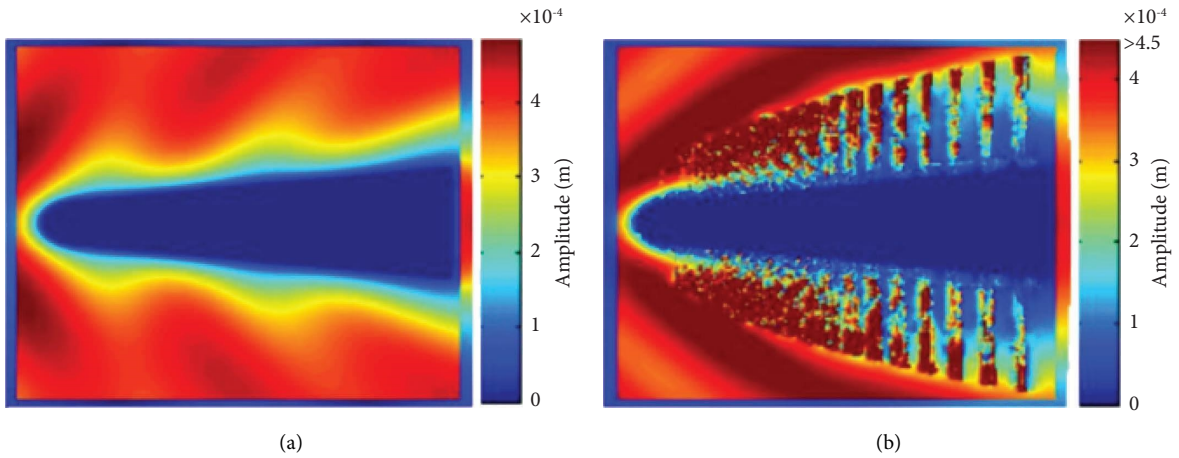

Figure 11: Continued.

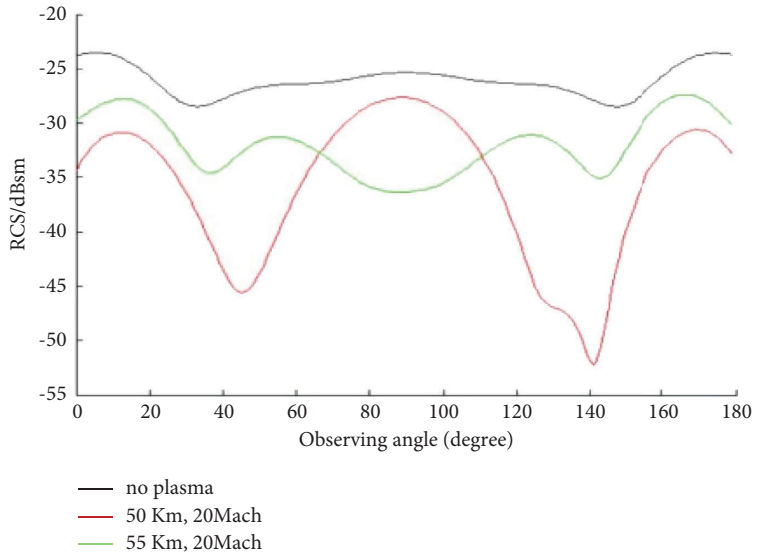

(c)

Figure 11: The amplitude and bistatic RCS at 4.0 GHz.

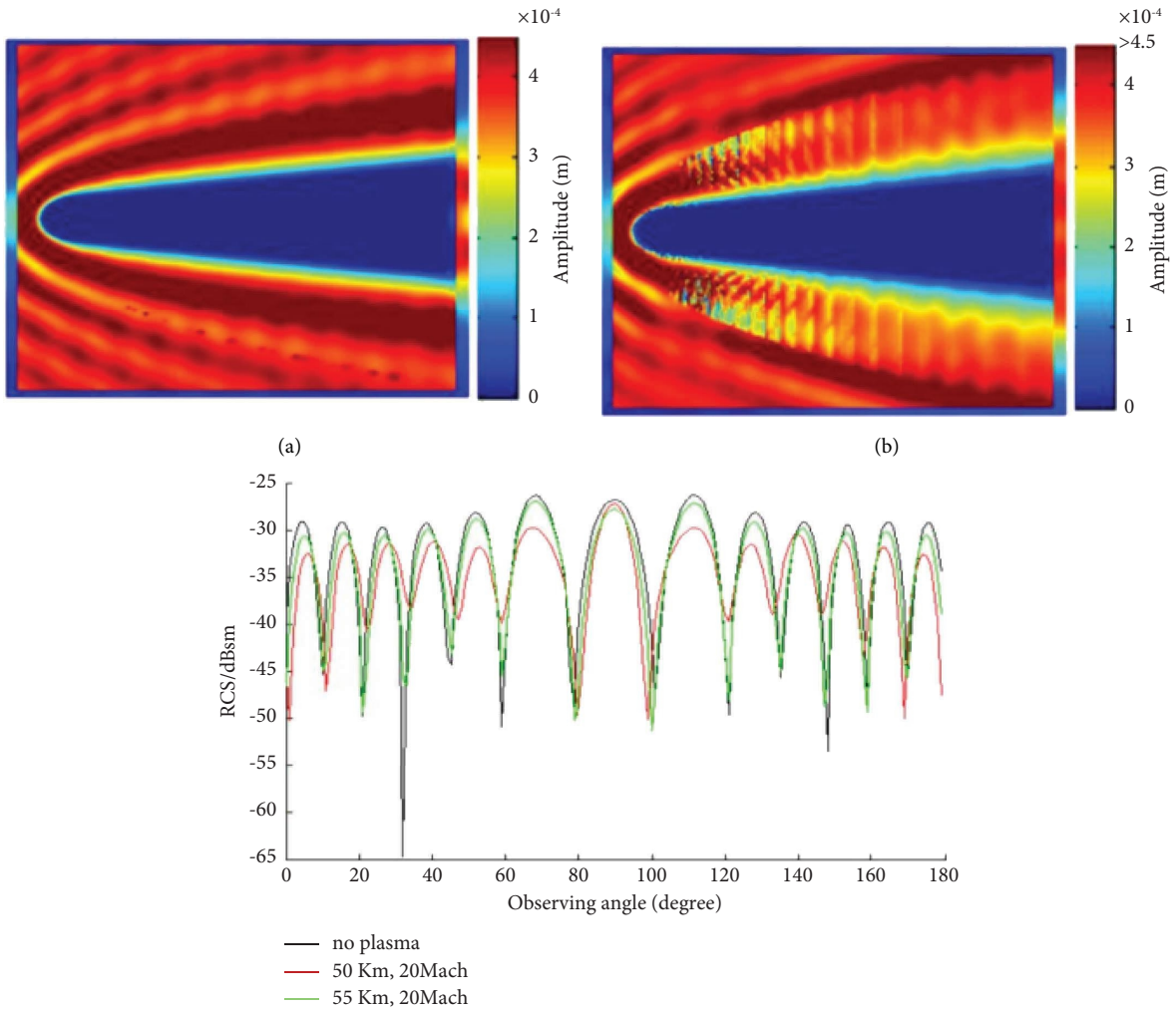

(c)

Figure 12: The amplitude and bistatic RCS at 15.0 GHz.

5. Conclusion

Most current calculation schemes for DGTD analysis are based on a single type of mesh scheme, which is inefficient when calculating no-uniform flow field. Here, we propose an asymmetrically mixed higher-order mesh DGTD method to address this problem. This method took into account the higher-order computational accuracy while reducing computation. The reliability of the asymmetrically mixed high-order mesh DGTD method is verified by plasma ball experiments. Compared with the single-type high-order mesh, the proposed method reduces the computational effort and has the advantage over the first-order mesh to further profile the target. We study the influence between plasma flow of hypersonic vehicle and electromagnetic wave from the perspective of amplitude and scattering for the first time. More research ideas are proposed for studying the relationship between flight height and electromagnetic wave frequency.

This article has considered an asymmetrically mixed higher-order mesh DGTD method for only two types of mesh, the Lagrange high-order mesh with 27 nodes and the Serendipity high-order mesh with 20 nodes, for a type of transition unit. This method currently applies only to these two kinds of mesh. Nevertheless, it can also be adapted for other types of Lagrange grids and Serendipity grids and constructs corresponding transition unit. Moreover, when the order of the magnitude gradient of nonuniform medium parameters is relatively large, different types of mesh need to be constructed according to the gradient values. This will be investigated in future work.

Data Availability

The processed data are available from the corresponding author upon request. The data for other figures in this paper used to support the findings of this study are also available from the corresponding author upon request.

Conflicts of Interest

The authors declare that they have no conflicts of interest.

Acknowledgments

This work was supported by the National Key Research and Development Program of China under grant no. 6142411203109.

References

[1] J. Xu, B. Bai, C. Dong, Y. Dong, Y. Zhu, and G. Zhao, "Evaluations of plasma stealth effectiveness based on the probability of radar detection," *IEEE Transactions on Plasma Science*, vol. 45, no. 6, pp. 938–944, 2017.

[2] J. P. Rybak and R. Churchill, "Progress in reentry communications," *IEEE Transactions on Aerospace and Electronic Systems*, vol. 7, pp. 879–894, 1971.

[3] F. Li, M. Choudhari, C.-L. Chang, and J. White, "Effects of injection on the instability of boundary layers over hypersonic configurations," *Physics of Fluids*, vol. 25, no. 10, pp. 104–107, 2013.

[4] H. Sun, J. Wang, Y. Han et al., "Backward scattering characteristics of a reentry vehicle enveloped by a hypersonic flow field," *International Journal of Antennas and Propagation*, vol. 2018, Article ID 5478580, 14 pages, 2018.

[5] W. Rusch and C. Yeh, "Scattering by an infinite cylinder coated with an inhomogeneous and anisotropic plasma sheath," *IEEE Transactions on Antennas and Propagation*, vol. 15, no. 3, pp. 452–457, 1967.

[6] F. Mitchell, W. Mahaffey, and R. Jacob, "Modeling plasma effects on radar cross section of reentry vehicles," *IBM Journal of Research and Development*, vol. 13, no. 4, pp. 468–474, 1969.

[7] J. Wang, D. Zhang, C. Liu et al., "Unipic code for simulations of high power microwave devices," *Physics of Plasmas*, vol. 16, no. 3, 2009.

[8] Y. Wang, J. Wang, Z. Chen, G. Cheng, and P. Wang, "Three-dimensional simple conformal symplectic particle-in-cell methods for simulations of high power microwave devices," *Computer Physics Communications*, vol. 205, pp. 1–12, 2016.

[9] S.-H. Liu and L.-X. Guo, "Analyzing the electromagnetic scattering characteristics for 3-d inhomogeneous plasma sheath based on po method," *IEEE Transactions on Plasma Science*, vol. 44, no. 11, pp. 2838–2843, 2016.

[10] A. C. Yucel, L. J. Gomez, and E. Michielssen, "Internally combined volume-surface integral equation for em analysis of inhomogeneous negative permittivity plasma scatterers," *IEEE Transactions on Antennas and Propagation*, vol. 66, no. 4, pp. 1903–1913, 2018.

[11] A. Scarabosio, J. L. A. Quijano, J. Tobon et al., "Radiation and scattering of em waves in large plasmas around objects in hypersonic flight," *IEEE Transactions on Antennas and Propagation*, vol. 70, no. 6, pp. 4738–4751, 2022.

[12] Y. Zhong-cai and S. Jia-ming, "Collisional, nonuniform plasma sphere scattering calculation by fdtd employing a drude model," *International Journal of Infrared and Millimeter Waves*, vol. 28, no. 11, pp. 987–992, 2007.

[13] W. Chen, L. X. Guo, and J. T. Li, "Research on the fdtd method of scattering effects of obliquely incident electromagnetic waves in time-varying plasma sheath on collision and plasma frequencies," *Physics of Plasmas*, vol. 24, no. 4, Article ID 042102, 2017.

[14] Y. Chang, W. F. Chen, and W. U. Qi-Fen, "Analysis of the scattering characteristic for the hypersonic flow field with near wake region of sphere," *Journal of National University of Defense Technology*, vol. 31, pp. 5–10, 2009.

[15] J. Chen and J. Wang, "A three-dimensional semi-implicit fdtd scheme for calculation of shielding effectiveness of enclosure with thin slots," *IEEE Transactions on Electromagnetic Compatibility*, vol. 49, no. 2, pp. 354–360, 2007.

[16] J. Chen and J. Wang, "Three-dimensional dispersive hybrid implicit–explicit finite-difference time-domain method for simulations of graphene," *Computer Physics Communications*, vol. 207, pp. 211–216, 2016.

[17] P. Wu, H. Yu, Y. Xie, H. Jiang, and T. Natsuki, "Efficient enhanced hybrid implicit-explicit procedure to gyrotropic plasma in open regions with fine geometry details along single direction," *IEEE Access*, vol. 9, pp. 77079–77089, 2021.

[18] J. Chen and J. Wang, "A novel wcs-fdtd method with weakly conditional stability," *IEEE Transactions on Electromagnetic Compatibility*, vol. 49, no. 2, pp. 419–426, 2007.

[19] J. Chen, J. Tan, and X. Yu, "Using wcs-fdtd method to study the plasma frequency selective surface," *IEEE Access*, vol. 7, pp. 152473–152477, 2019.

[20] Y. Takahashi, R. Nakasato, and N. Oshima, "Analysis of radio frequency blackout for a blunt-body capsule in atmospheric reentry missions," *Aerospace*, vol. 3, no. 1, p. 2, 2016.

[21] B. Cockburn, G. E. Karniadakis, and C.-W. Shu, *The Development of Discontinuous Galerkin Methods*, Springer, Berlin, Germany, 2000.

[22] S. Yan, A. D. Greenwood, and J.-M. Jin, "Modeling of plasma formation during high-power microwave breakdown in air using the discontinuous galerkin time-domain method," *IEEE Journal on Multiscale and Multiphysics Computational Techniques*, vol. 1, pp. 2–13, 2016.

[23] Q. Yang, B. Wei, L. Li, and D. Ge, "Analysis of the calculation of a plasma sheath using the parallel so-dgtd method," *International Journal of Antennas and Propagation*, vol. 2019, Article ID 7160913, 9 pages, 2019.

[24] H. Wang, L. Xu, B. Li, S. Descombes, and S. Lanteri, "An exponentialbased dgtd method for modeling 3-d plasma-surrounded hypersonic vehicles," *IEEE Transactions on Antennas and Propagation*, vol. 68, no. 5, pp. 3847–3858, 2020.

[25] L. Kou, D. Peng, X. Li, and H. Yang, "An arbitrary high-order hexahedrons generation technology for dgtd algorithm," in *Proceedings of the ISAPE2012*, pp. 991–994, IEEE, Xi'an, China, October 2012.

[26] J. Liu, Z. Fan, D. Ding, and R. Chen, "High-order dgtd for solving em scattering from hypersonic aircraft with plasma sheath," in *Proceedings of the 2019 Photonics and Electromagnetics Research Symposium-Fall (PIERS-Fall)*, pp. 1845–1852, IEEE, Xiamen, China, December 2019.

[27] Z. Xiao, B. Wei, and D. Ge, "A hybrid mesh dgtd algorithm based on virtual element for tetrahedron and hexahedron," *IEEE Transactions on Antennas and Propagation*, vol. 69, pp. 2242–2248, 2020.

[28] P. A. Gnoffo, R. N. Gupta, and J. L. Shinn, *Conservation Equations and Physical Models for Hypersonic Air Flows in thermal and Chemical Nonequilibrium*, Nasa Tp, Washington DC, USA, 1989.

[29] J.-W. Qian, H.-L. Zhang, and M.-Y. Xia, "Modelling of electromagnetic scattering by a hypersonic cone-like body in near space," *International Journal of Antennas and Propagation*, vol. 2017, Article ID 3049532, 11 pages, 2017.

[30] N. V. Ardeljan, G. S. Bisnovatyi–kogan, and K. V. Kosmachevskii, "Simulation of the collapse of a rotating gas cloud on triangular reconstructing Lagrangian grid," *Astronomical and Astrophysical Transactions*, vol. 10, no. 4, pp. 341–355, 1996.

[31] M. S. Shephard, S. Dey, and J. E. Flaherty, "A straightforward structure to construct shape functions for variable p-order meshes," *Computer Methods in Applied Mechanics and Engineering*, vol. 147, no. 3-4, pp. 209–233, 1997.

[32] S. Reaz Ahmed, M. Khan, K. Islam, and M. Wahhaj Uddin, "Analysis of stresses in deep beams using displacement potential function," *Journalinstitution Of Engineers India Part Mc Mechanical Engineering Division*, vol. 77, pp. 141–147, 1996.

[33] J. P. Rybak and R. Churchill, "Progress in reentry communications," *IEEE Transactions on Aerospace and Electronic Systems*, vol. 7, no. 5, pp. 879–894, 1971.